IEEE Access
Multidisciplinary ⋮ Rapid Review ⋮ Open Access Journal

Received 29 December 2023, accepted 21 January 2024, date of publication 1 February 2024, date of current version 9 February 2024.

Digital Object Identifier 10.1109/ACCESS.2024.3361309

RESEARCH ARTICLE

Design and Implementation of Load Network Time Constant Computation Based Solar Active Power Filters Cum Injector for Industrial Loads/Grids

P. MAHESH REDDY, (Member, IEEE), BAIBHAV KUMAR GUPTA, AND K. RAMACHANDRA SEKHAR, (Member, IEEE)
Indian Institute of Technology Ropar, Rupnagar 140001, India

Corresponding author: P. Mahesh Reddy (2018eez0008@iitrpr.ac.in)

This work was supported in part by the "Ministry of Electronics and Information Technology (MeiTy)" under Grant 25(2)/2021-ESDA, and in part by the "Science and Engineering Research Board (SERB)" under Grant CRG/2020/002958.

ABSTRACT This work proposes an efficient integration method of solar energy with industrial nonlinear loads, accounting for dynamic variations in solar power and load harmonic profiles. The involved dynamics necessitate that the solar interface front-end inverters be equipped to handle both harmonic distortions and active power injection characteristics simultaneously. In this work, an instantaneous load and source characteristic mapping is proposed for the solar-interfaced front-end inverter operated as a shunt active power filter cum active power injector in order to accommodate the dynamic variations of the source and load. As per requirement, to separate the load-demanded and switching harmonics, a new load network time constant-based passive filter design diverging from traditional passive filter design methods is demonstrated. Further, a comprehensive explanation of the current controller modeling methodology is elaborated, considering the essential bandwidth required for proficiently managing load-demanded harmonics in both grid injection and drawing modes of operation. Later, in grid injection mode, the influence of grid and system impedance interactions on the power quality is analyzed for weak grid scenarios to derive the requisite bandwidth conditions to ensure resilient power transfer. Subsequently, the experimental validation of the solar interfaced shunt active power filter (SISAPF) with active power injection capability is carried out in both grid power drawing and injection modes, demonstrating the effectiveness of the enhanced bandwidth in handling load-demanded harmonics and solar power dynamic variations.

INDEX TERMS EV charging infrastructure, load time constant, non-linear loads, passive filter design, shunt active filter, solar inverter, system bandwidth, three-phase inverter.

I. INTRODUCTION

With growing awareness of the implications of global warming, countries worldwide are actively pursuing strategic measures to curtail their greenhouse gas emissions. A highly effective strategy involves integrating renewable energy sources such as solar power into their energy grids [1], [2], [3], [33]. However, the integration process faces significant technical challenges, including the intermittent nature of solar energy and fluctuations in industrial loads such as like drives and electric arcs. Additionally, it's essential to recognize that industrial loads can introduce disruptions into the power grid, such as injecting harmonics and oscillations, leading to issues like power quality and voltage instability [5] and [6]. To overcome these challenges, it is crucial to develop power converters capable of efficiently injecting power into the grid,

The associate editor coordinating the review of this manuscript and approving it for publication was Xiaodong Liang.

effectively managing disturbances, and ensuring compliance with IEEE standards [7] to maintain a specific level of grid quality (%THD).

Hence, researchers [8], [9], [10], [11], [12] have introduced passive and active power filters to regulate current harmonics and maintain them within acceptable limits. This approach significantly elevates the overall power supply quality. In the domain of passive filters, [8], [9], [10] discussed the use of traditional LC and LCL filters to address harmonic currents. These passive filters have a straightforward design and are cost-effective, but bulky, heavy, and usually calibrated to address specific predominant harmonics [10]. Furthermore, their compensatory capacity is fixed and heavily dependent on the impedance of the connected electrical network, which may result in undesirable resonance problems [8].

On the other hand, within the active filter domain, shunt active filters (SAFs) are a well-established solutions that have been extensively studied for mitigating predominant harmonics [10], [11], [12]. However, designing SAFs necessitates a thorough evaluation of factors, including source availability, converter topology, control methods, and output filters, to tackle harmonic issues efficiently [13]. These active filters are directly linked to the load or at the Point of Common Coupling (PCC). The design principles for SAFs focus on attaining a sinusoidal current pattern in the power grid by extracting information about load current harmonics to synthesize a reference signal for the controller [12]. These harmonics can be extracted in SAFs through various methods, including stationary reference frame techniques [14] and [15], synchronous reference frame methods [16], [17], [18], or Fourier transform methods [22]. The effectiveness of SAF design through these extraction methods is optimized when the controller possesses sufficient bandwidth [19]. Inadequate controller bandwidth in SAFs can result in the undesirable introduction of notches in the injected grid current, further compromising the overall power quality of the grid as highlighted in [20] and [21]. Consequently, Various controller models with diverse harmonic compensation capabilities have been investigated, as evident in [23], [24], [25], [26], [27], [28], and [29]. However, the control methods showcased thus far have not considered the influence of the load's passive impedance and load current gradients in the determination of the controller's bandwidth [19]. To ensure the development of an accurate controller, it is imperative to take into account the load's passive impedance and the fluctuations in load current. This thoughtful consideration allows for the choice of minimum inductor values, equipping the active filter to effectively reduce harmonics and enhance the quality of the grid current.

In addition to precise controller modeling, the controller's bandwidth is also influenced by the converter filter design of the SAF [32]. Previous researchers have designed the passive filter with consideration for the current ripple in the output of the SAF, ensuring the provision of necessary load harmonics while simultaneously mitigating switching harmonics, as indicated in [30], [31], and [32]. In [20], the passive filter is specifically designed to efficiently eliminate switching harmonics while ensuring no impedance is added to the load-demanded harmonics. The given literature introduces a design approach that notably boosts the overall system bandwidth in comparison to conventional ripple-based filter designs. However, it falls short of delivering a perfectly sinusoidal current to the grid [20]. The reason behind this is the omission of the load's passive impedance and variations in load current gradients during the design of the passive filter. This omission results in unwanted disruptions in the grid current, further deteriorating the overall power quality.

The literature provided thus far has predominantly focused on supplying load harmonics using SAF, with limited attention given to the simultaneous injection of active power alongside harmonics supply [19]. As energy demands continue to rise, the need for solar interface active filters in nonlinear load infrastructures is growing [24]. These filters are expected to support active power injection into the grid while managing load-demanded harmonics. However, a notable challenge arises during active power injection due to the interaction between passive filter inductance and grid inductance. This interaction diminishes the short circuit ratio, leading to a weaker grid scenario [4]. This underscores the importance of designing the right passive filter and achieving the corresponding controller bandwidth to improve power quality in weak grid conditions. In [34] and [35], stability issues pertaining to weak grids are tackled by employing a synchronous reference frame-based model to depict the interactions between the grid and system impedance. The analysis reveals that modifying the bandwidth of the phase lock loop (PLL) notably impacts the system's capability to reject power harmonics [36]. However, it comes at the expense of compromising the dynamic response. Therefore, modifying the PLL bandwidth is not feasible as it restricts some of the load-demanded harmonics, leading to poor power quality, which contradicts the primary objective of SAF to provide the harmonics demanded by the load.

Subsequent researchers have suggested virtual feed-forward loop compensation techniques to adjust the control loop parameters based on network impedance [36]. Nevertheless, these feed-forward loops introduce positive feedback, necessitating additional precautions to maintain system stability [4]. Later, researchers recommended the use of lead-lag compensators and notch filters specifically designed to mitigate power harmonics, ultimately enabling the delivery of high-quality power in weak grid scenarios. These techniques aim to enhance the quality of power supplied to weak grids but have restricted applicability since they primarily address frequency variations at the PCC. Furthermore, these methods frequently require additional sensors and complex algorithms. A recent study outlined in [4] demonstrated that properly tuning the gain of the PI controller could effectively reduce existing harmonics in weak grid scenarios. This reduction was achieved through precise modeling of

the weak grid scenario, taking into account the interactions between system and network impedance [4]. However, it's important to note that these studies are solely focused on active power injection into the grid and do not address the supply of harmonics demanded by nonlinear loads.

Recognizing the crucial need for designing the right passive filter for solar interface inverters, especially for shaping grid power quality, this study introduces a novel passive filter design methodology. This methodology is based on the computation of instantaneous load time constants at various power processing instances, considering both load and source dynamics. The active filter designed in this context is required to serve a dual role by handling harmonics from nonlinear loads and injecting active power into the grid, even in weak grid scenarios. Furthermore, this proposed methodology sheds light on the substantial relationship between passive filter bandwidth and its capability to attenuate switching frequencies while still accommodating permissible load-demanded harmonics. In addition, the study comprehensively explains the approach for modeling and adjusting the current controller. This process involves monitoring the load network's time constant under different source and load power conditions and determining the bandwidth to manage load-demanded harmonics effectively. The SiSAPF system can also operate in grid power injection and drawing modes depending on the available solar power and the demanded load power. In the grid-injected mode, where interactions between grid impedance and network impedance result in power oscillations at the fundamental frequency, the study suggests establishing appropriate controller gain boundaries by evaluating interactive time constants.

II. THE SOLAR INTERFACED SHUNT ACTIVE POWER FILTER

The schematic featured in Fig. 1 illustrates the Solar interfaced Shunt Active Power Filter (SiSAPF), a system thoughtfully designed to serve a dual purpose. It effectively addresses the harmonics demanded by the load while seamlessly integrating solar power into the AC network. The proposed system comprises a three-phase inverter integrated with solar panels, establishing a connection with the AC power network. This three-phase inverter is strategically positioned at the Point of Common Coupling (PCC), where it links the grid and nonlinear loads, as depicted in Fig. 1. A passive inductor, denoted as L_f, is connected to the inverter's output terminals. The primary function of this passive inductor is to mitigate switching harmonics while facilitating the passage of harmonics required by the load. The importance of filter inductance design lies in establishing an effective bandgap between these harmonics. This design aspect plays a crucial role in achieving the desired power quality in the grid. Therefore, in the upcoming sections, this paper delves into the meticulous process of designing an efficient passive filter using load network time constant computation, comparing it with conventional ripple-based filter design methods.

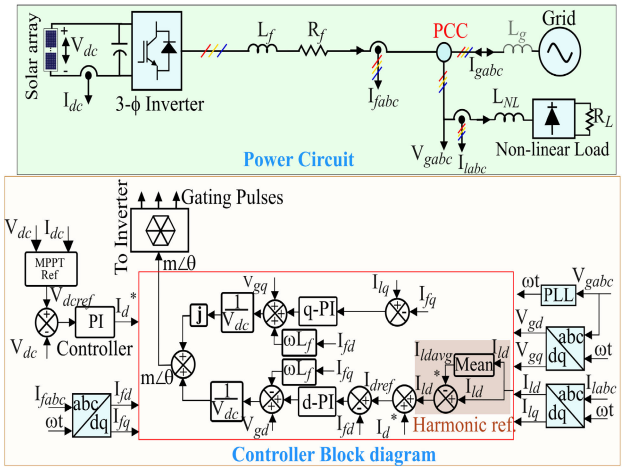

FIGURE 1. The solar interfaced shunt active power filter schematic with control diagram.

III. THE PROPOSED LOAD NETWORK TIME CONSTANT COMPUTATION BASED PASSIVE INDUCTANCE DESIGN METHOD

The design of passive inductance (L_f) ensures the optimal performance of SiSAPF in delivering load harmonics while attenuating the switching frequency component. The following section thoroughly elucidates a comprehensive method for determining the minimum and maximum inductance values.

A. MINIMUM FILTER INDUCTANCE DESIGN

To establish the minimum inductance value necessary for efficient harmonics management and the suppression of the switching frequency component, configure the three-phase inverter to solely supply active power to the load, which is represented by resistance $\mathbb{R}$ (where $\mathbb{R} = \frac{V_g}{I_g}$). This configuration is illustrated in the single-line diagram as shown in Fig. 2, facilitating the calculation of the required back electromotive force (emf) at the switching frequency across the passive inductance and resistance. The voltage across resistor $\mathbb{R}$, due to the switching frequency current, must match the emf produced by the inductor (e_{sw}), as depicted in Fig. 2. This relationship is expressed as:

$$e_{f_{sw}} = \mathbb{R} i_{fsw} = 2\pi f_{sw} L_{f_{min}} i_{fsw} \tag{1}$$

The information regarding the calculated back emf is pivotal in eliminating the current component generated by the switching frequency. Consequently, the minimum filter inductance can be determined using Equation. 2.

$$L_{f_{min}} = \frac{\mathbb{R}}{2\pi f_{sw}} \tag{2}$$

$$\mathbb{R} = 2 * \pi * f_{sw} * L_{f_{min}} \tag{3}$$

As shown in Fig. 2, the inductor produces varying back-emf across a range of frequencies, spanning from the fundamental frequency to the switching frequency.

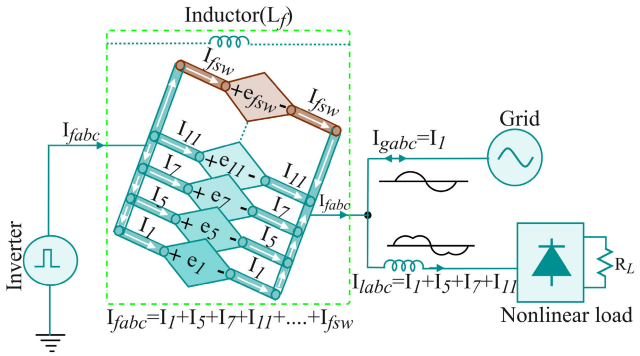

FIGURE 2. The SiSAPF's network single line diagram with the realization of filter inductance as a decomposed harmonic back-EMFs.

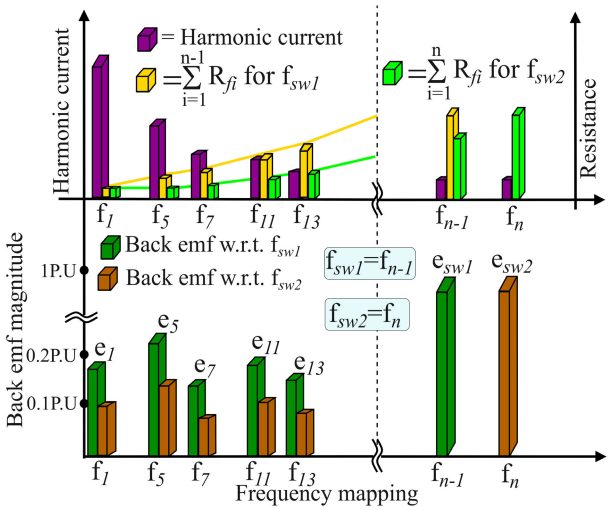

FIGURE 3. The variation of the current harmonics along with the offered resistance and corresponding back emf offered by the filter inductor (L_f) at two frequencies f_{sw1} and f_{sw2}.

To effectively accommodate the harmonics required by the load, it's crucial that $L_{f_{min}}$ does not contribute any back emf to these harmonics. The amplitude of the back emf imparted to each harmonic depends on the filter inductance and can be expressed as follows:

$$\begin{aligned} EMF_{inductor} &= e_1 + e_5 + e_7 + e_{11} + \ldots. + e_{fsw} \\ &= i_1.\mathscr{R}_1 + i_5.\mathscr{R}_5 + i_7.\mathscr{R}_7 + i_{11}. \\ &\quad \mathscr{R}_{11} + \ldots\ldots. + i_{fsw}.\mathbb{R} \end{aligned} \tag{4}$$

The value of $(\mathscr{R}_1, \mathscr{R}_5, \mathscr{R}_7 \ldots\ldots \mathbb{R})$ is obtained using Equ.(3).

$$\mathscr{R}_1 = 2.\pi f_1 L_{f_{min}};\ \mathscr{R}_5 = 2.\pi f_5 L_{f_{min}} \ldots \tag{5}$$

In this context, the impedance's $\mathscr{R}_1, \mathscr{R}_5, \mathscr{R}_7$, and so on are frequency-dependent, varying in magnitude relative to multiples of the fundamental frequency. This change is visually represented in the top trace of Fig. 3, using yellow and green colors to differentiate between two distinct switching frequencies, namely, f_{sw1} and f_{sw2}. As the inverter's

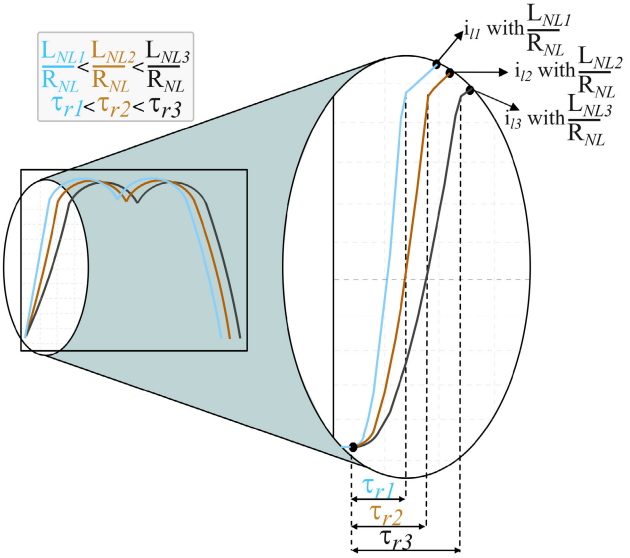

FIGURE 4. The non-linear load current profile with change in network inductance L_{NL}.

operational switching frequency transitions from f_{sw1} to f_{sw2}, the computed impedance values, in accordance with Equation(5), diminish. This leads to reduced impedances, depicted in green, for individual current harmonics, indicated in violet, as observed in the top trace of Fig. 3. Moreover, the corresponding back emf for individual current harmonics at these two unique operational switching frequencies, f_{sw1} and f_{sw2}, is visualized in the bottom trace of Fig. 3. It's evident that the provided back emf consistently registers a slightly lower value, approximately 0.1 to 0.3 per unit (PU), compared to the back emf at the switching frequency. This observation underlines the significance of maintaining minimal back emf for the harmonics required by the load, ensuring that the designed minimum passive filter inductance is capable of delivering these harmonics without attenuation. Simultaneously, the calculated inductance value defines the time constant of the SiSAPF system as follows:

$$\tau_{sys} = \frac{L_{f_{min}}}{\mathbb{R}} \tag{6}$$

B. MAXIMUM FILTER INDUCTANCE DESIGN

To establish the maximum inductance value, it's crucial to evaluate the required bandwidth by taking into account the load network time constant. This time constant is dependent on factors such as the load network's per-phase equivalent resistance (R_{NL}) and inductance (L_{NL}), as visually represented in Fig. 4. The load network time constant (τ_n) is defined as follows

$$\tau_n = \frac{L_{NL}}{R_{NL}} \tag{7}$$

where, the method for obtaining the R_{NL} value is detailed in the appendix.

The connection between the load network time constant and the rate of load current rise is defined by Equ.(8).

$$2\pi f_{BW} = \frac{1}{\tau_r} = \frac{1}{2.197\tau_n} \tag{8}$$

This relationship shows that the per-phase load current rise time is approximately 2.197 times the load network time constant (τ_n). Additionally, it is evident from Fig. 4 that a reduction in filter inductance results in a shorter rise time for the load current while the load power remains constant. The understanding of a shorter rise time plays a pivotal role in the design of a SiSAPF passive filter, aimed at achieving a broader bandwidth than the load network. This objective is attained through a systematic design approach for the passive filter, with a particular emphasis on the load network time constant (τ_n) and the SiSAPF system time constant (τ_{sys}) as essential parameters. To effectively manage the complete spectrum of load-demanded harmonics without any reduction, it is crucial to guarantee that the SiSAPF system time constant (τ_{sys}) remains shorter than the load network time constant (τ_n). Consequently, the maximum values for the filter inductance can be determined based on the network time constant, and these values are as follows:

$$L_{f_{max}} = \tau_n.\mathbb{R} \tag{9}$$

The filter specifications, determined through Equation(9) for different load processing powers, are compared with traditional ripple-based filter design methods [20], as depicted in Fig. 5. It becomes evident that the innovative filter design effectively accommodates the load-demanded harmonics, ensuring a flawless sinusoidal grid current, unlike the conventional filter design methods. Conventional filter design methods take into account the inverter switching frequency and the magnitude of current ripple when designing passive filters for SAFs as depicted in Equation(10).

$$\begin{aligned}
L_f &= \frac{V_{dc}}{6F_{sw}\triangle I_{pp_{max}}} \quad Method-1 \\
L_f &= \frac{V_{dc}}{2\sqrt{6}F_{sw}\triangle I_{pp_{max}}} \quad Method-2 \\
L_f &= \frac{V_{dc}}{8F_{sw}\triangle I_{pp_{max}}} \quad Method-3 \\
L_f &= \frac{m_a V_{dc}}{12F_{sw}\triangle I_{pp_{max}}} \quad Method-4
\end{aligned} \tag{10}$$

It is worth noting that the conventional approach results in larger filter inductance sizes, as shown in Fig. 5, and fails to provide adequate bandwidth for the load-demanded harmonics. This leads to the introduction of unwanted notches in the grid current and, consequently, a degradation in the overall power quality of the grid, as displayed in Fig. 6. The reason for this is that these methods often overlook the impact of load passive impedance and variations in load current gradients when determining the passive filter inductance value.

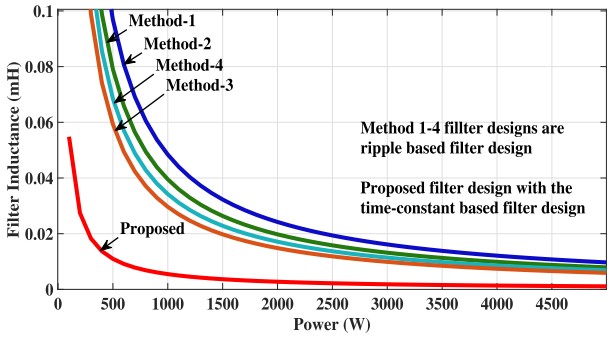

FIGURE 5. Comparison of filter design methods at different powers.

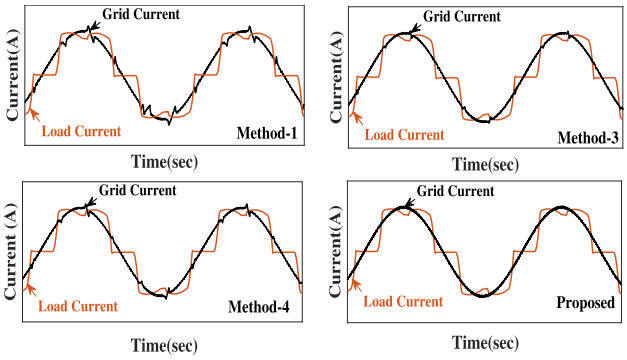

FIGURE 6. Comparison of grid currents for the load currents at different filter design methods.

Finally, taking into account the essential bandwidth and switching frequency attenuation criteria, the permissible range of filter inductance can be determined based on:

$$\frac{\mathbb{R}}{2\pi f_{sw}} \leq L_f \leq \tau_n \mathbb{R} \tag{11}$$

Following the modeling of filter inductance, it is essential to employ closed-loop modeling to enhance further the performance of the proposed SiSAPF system in delivering active power while managing load-demanded harmonics. This modeling approach aids in determining the appropriate controller gains for achieving the desired dynamic response and optimizing the overall system bandwidth. Further insights on closed-loop modeling are provided in the following section.

IV. THE SISAPF's CLOSED-LOOP CONTROLLER MODELING

This section focuses on the closed-loop controller modelling based on the synchronous reference frame (SRF). The objective is to attain the desired dynamic responses while managing load-demanded harmonics. In the SRF approach, the three-phase grid voltages are sensed at the Point of Common Coupling (PCC) to derive the synchronous voltage references (v_{gd} & v_{gq}).

$$v_{gd} = \frac{2}{3}(v_{ga}cos(\omega t) + v_{gb}cos(\omega t - 120^o)$$

$$+ v_{gc}cos(\omega t + 120^o)); \quad (12)$$

$$v_{gq} = \frac{-2}{3}(v_{ga}sin(\omega t) + v_{gb}sin(\omega t - 120^o) + v_{gc}sin(\omega t + 120^o)); \quad (13)$$

Here, ωt represents the grid voltage angle obtained through a phase-locked loop (PLL).

Subsequently, the three-phase nonlinear load currents (I_{la}, I_{lb}, and I_{lc}) are converted into a synchronous reference frame by employing the acquired grid voltage angle (ωt), as outlined below:

$$I_{ld} = \frac{2}{3}(I_{la}cos(\omega t) + I_{lb}cos(\omega t - 120^o) + I_{lc}cos(\omega t + 120^o));$$

$$I_{lq} = \frac{-2}{3}(I_{la}sin(\omega t) + I_{lb}sin(\omega t - 120^o) + I_{lc}sin(\omega t + 120^o)); \quad (14)$$

In this context, I_{la}, I_{lb} and I_{lc} represent the three-phase nonlinear load currents sensed before the diode bridge rectifier, as depicted in Fig. 1, and are subsequently converted to the synchronous reference frame as I_{ld} and I_{lq}. The load harmonics component information is then extracted by subtracting the fundamental component from the real component of the nonlinear load current, as outlined in Equation(15)

$$\begin{bmatrix} I_{ldh} \\ I_{lqh} \end{bmatrix} = \begin{bmatrix} I_{ld} - Avg(I_{ld}) \\ I_{lq} \end{bmatrix} \quad (15)$$

Subsequently, the reference for the current controller can be determined by combining the extracted load harmonics component with the photovoltaic active power component, as shown below:

$$\begin{bmatrix} I_{dref} \\ I_{qref} \end{bmatrix} = \begin{bmatrix} I_{ldh} + I_d^* \\ I_{lqh} \end{bmatrix} \quad (16)$$

where I_d^* represents the active power reference generated by the Maximum Power Point Tracking (MPPT) controller, as shown in Fig. 1. Moreover, Fig. 7 illustrates the typical variations of I_{ld} and I_{lq}. It's noteworthy that the rise time of I_{lq} precisely aligns with the load current rise time (τ_r), indicating that the load network's time constant (τ_n) information is inherently embedded in I_{qref}. Consequently, I_{qref} data alone is sufficient for determining the network time constant required to design the SiSAPF inductance and the associated closed-loop controller gains. Furthermore, the derived active power reference (I_{dref}) integrates the available photovoltaic active power with the load harmonics demand, allowing the SiSAPF network to operate in two modes based on available solar active power.

1) Mode-1 (Grid drawing power mode): When the available solar active power (PS) is less than or equal to the load demanded active power (P_L), i.e. ($P_S <= P_L$), the active power drawn from the grid can be calculated as P_{gd}=P_L-P_S.

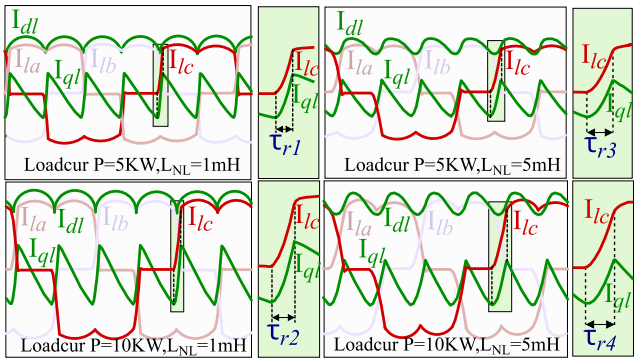

FIGURE 7. The variation of three phase nonlinear load currents and corresponding real and reactive component (I_{dref} and I_{qref}) profiles in SRF at different filter inductance and network power.

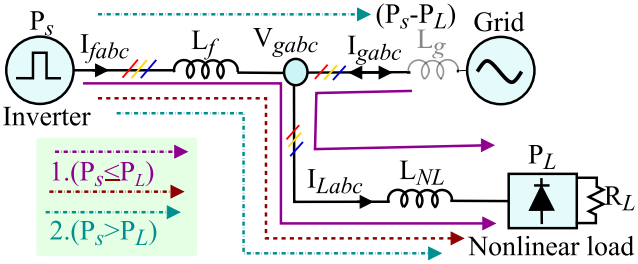

FIGURE 8. The single line diagram of the power network demonstrates the power interaction between SiSAPF, grid, and nonlinear load.

2) Mode-2 (Grid Injection power mode): $P_S > P_L \implies$, the active power injected to the grid can be calculated as P_{gi} =P_S-P_L;

The controller gain modeling for mode-1 and mode-2 is described in the subsequent subsection by monitoring the power and its associated time constant.

A. MODE-1 OPERATION

During this mode of operation, the equivalent resistance (R_s) corresponding to the available solar energy processed by SiSAPF can be identified as:

$$R_s = \frac{v_{gd}}{I_{fd}} \quad (17)$$

Here, v_{gd} represents the grid voltage, and I_{fd} is the grid-injected current in the d-domain. By utilizing the identified resistance (R_s) and system inductance (L_f), the system's transfer function can be obtained by identifying the rate of change in reference current as follows:

$$\frac{dI_{dref}}{dt} = \frac{2}{3}((\frac{v_{ga}}{L_f} - \frac{R_s}{L_f}i_{fa})cos(\omega t) + (\frac{v_{gb}}{L_f} - \frac{R_s}{L_f}i_{fb}) cos(\omega t - 120°) + (\frac{v_{gc}}{L_f} - \frac{R_s}{L_f}i_{fc})cos(\omega t + 120°)) + \omega I_{qref}$$

$$\frac{dI_{qref}}{dt} = \frac{-2}{3}((\frac{v_{ga}}{L_f} - \frac{R_s}{L_f}i_{fa})sin(\omega t) + (\frac{v_{gb}}{L_f} - \frac{R_s}{L_f}i_{fb}) sin(\omega t - 120°) + (\frac{v_{gc}}{L_f} - \frac{R_s}{L_f}i_{fc})sin(\omega t + 120°)) - \omega I_{dref} \quad (18)$$

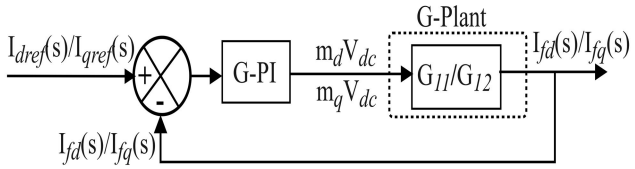

FIGURE 9. The signal flow diagram consolidated the plant model and controller.

Here, i_{fa}, i_{fb}, and i_{fc} represent the SiSAPF three-phase currents, while v_{ga}, v_{gb}, and v_{gc} denote grid voltages, as illustrated in Figure 1. Substituting (12) and (13) into Equation (18) yields:

$$\frac{dI_{dref}}{dt} = \frac{v_{gd}}{L_f} - \frac{R_s}{L_f} I_{dref} + \omega . I_{qref} \tag{19}$$

$$\frac{dI_{qref}}{dt} = \frac{v_{gq}}{L_f} - \frac{R_s}{L_f} I_{qref} - \omega . I_{dref} \tag{20}$$

The derived (19) and (20) can be expressed in the form of state space model as $\dot{x} = Ax + Bu$ and $y = Cx + Du$:

$$\begin{bmatrix} \frac{dI_{dref}}{dt} \\ \frac{dI_{qref}}{dt} \end{bmatrix} = \begin{bmatrix} \frac{-R_S}{L_f} & \omega \\ -\omega & \frac{-R_S}{L_f} \end{bmatrix} \begin{bmatrix} I_{dref} \\ I_{qref} \end{bmatrix} + \begin{bmatrix} \frac{V_{dc}}{L_f} & 0 \\ 0 & \frac{V_{dc}}{L_f} \end{bmatrix} \begin{bmatrix} m_d \\ m_q \end{bmatrix} \tag{21}$$

$$\begin{bmatrix} I_{fd} \\ I_{fq} \end{bmatrix} = \begin{bmatrix} 1 & 0 \\ 0 & 1 \end{bmatrix} \begin{bmatrix} I_{dref} \\ I_{qref} \end{bmatrix} \tag{22}$$

where, $V_{gd} = m_d * V_{dc}$ and $V_{gq} = m_q * V_{dc}$.

Furthermore, the transfer function can be derived from the state-space equation in the following form:$[Y(s) = (C(SI - A)^{-1}B + D)$

$$\begin{bmatrix} I_{fd} \\ I_{fq} \end{bmatrix} = \begin{bmatrix} G_{11} & G_{12} \\ G_{21} & G_{22} \end{bmatrix} \begin{bmatrix} m_d \\ m_q \end{bmatrix} \tag{23}$$

The derived G_{11} and G_{22} represents the $d-$ loop and $q-$ loop plant transfer functions as shown in Fig.9.

The plant transfer function is described as

$$G_{11} = \quad G_{22} = \frac{(sL_f + R_S)}{s^2 L_f^2 + 2L_f R_S s + R_S^2 + \underbrace{(\omega L_f)^2}_{\approx 0}} \tag{24}$$

Here, ωL_f represents the cross-coupling term. As this coupling term is compensated in the feed-forward loop, as shown in Figure 1, the plant's transfer function can be simplified as:

$$G_{11} = G_{22} = \frac{1}{(sL_f + R_S)} \tag{25}$$

As demonstrated in Equation (25), the value of L_f determines the open-loop response of the plant. The Bode plot of the plant, with L_f calculated using both the conventional ripple-based method and the proposed time constant-based method, is shown in Fig. 10. From the Bode plot and root locus plot in Fig. 10, it is evident that the inductance computed using the method described in this work provides a wider bandwidth compared to the ripple-based filter design method.

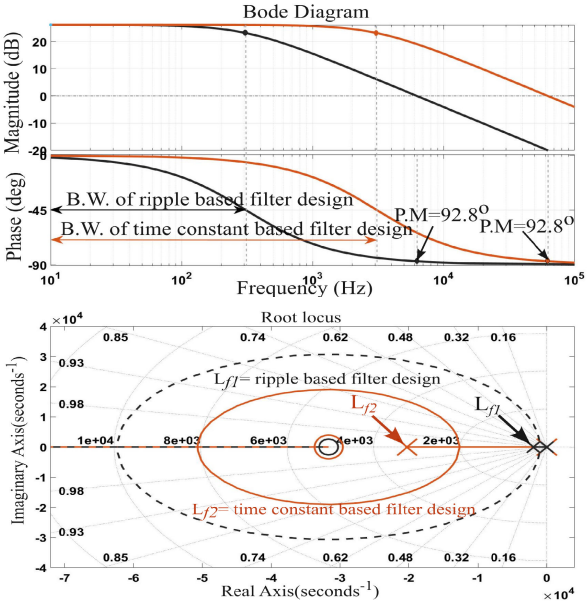

FIGURE 10. The Bode diagram and Root locus of SiSAPF's open-loop transfer function with the variation of the filter inductance.

Later, in order to analyze the system's dynamic response effectively, it is essential to determine the closed-loop transfer function. Initially, the open-loop transfer function of the plant is established by combining the transfer functions of the PI controller and the plant, as shown below:

$$G_{PI} = K_P + \frac{K_I}{s}; \quad G_{open} = G_{PI} * G_{plant} \tag{26}$$

$$G_{open} = \frac{K_P}{sL_f} . (s + \frac{K_I}{K_P}) . (\frac{1}{s + \frac{R_S}{L_f}}) \tag{27}$$

Furthermore, the closed-loop transfer function can be expressed as follows:

$$G_{closed} = \frac{G_{open}}{1 + G_{open}} \tag{28}$$

Using the closed-loop transfer function, the controller gains can be determined as follows:

$$K_P = \frac{L_f}{\tau_s}; K_I = \frac{R_S}{L_f} . K_P; \tau_s = \frac{L_f}{K_P} \tag{29}$$

As per Equation (29), it is evident that the value of K_P at a given L_f determines the system's dynamic response. The step response of the closed-loop system at different K_P values is depicted in Fig. 11. It is clear from Fig. 11 that an increase in K_P leads to an improved dynamic response as the system time constant (τ_s) decreases. Therefore, selecting a suitable K_P value that satisfies $\tau_s \leq \tau_n$ is essential to smoothly process the load-demanded harmonics along with active power injection into the power network. However, increasing gain values cause the controller's zeros to shift towards the right-hand side of the complex plane, as shown in Fig. 12. Fig. 12 makes it evident that the controller zeros are moving towards

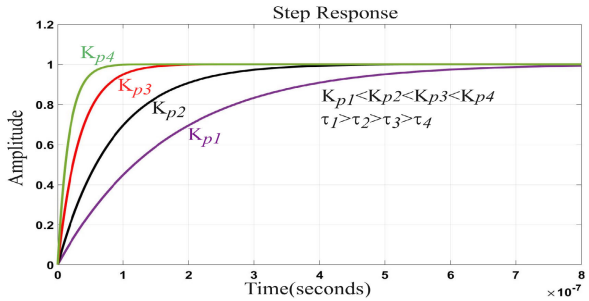

FIGURE 11. Step response SiSAPF's closed-loop transfer function with varying K_p.

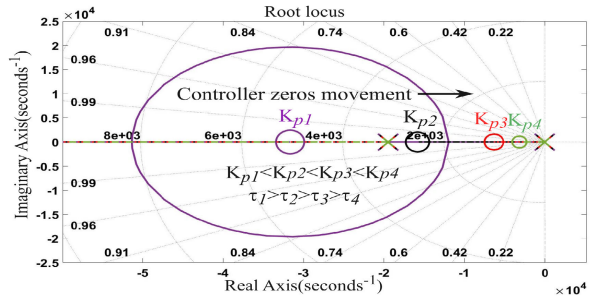

FIGURE 12. Root locus of SiSAPF's open-loop transfer function with varying K_p.

an unstable region. Hence, choosing controller gains within acceptable limits is crucial to ensure stable system operation. The effect of the controller gains on grid current in terms of % THD for processing the inverter power into the grid and load is discussed in the following section.

B. THE SELECTION OF CONTROLLER GAINS BASED ON LOAD NETWORK TIME CONSTANT

Further, in this subsection, the controller gains selection based on the determined load network time constant for accomplishing the maximum possible closed-loop bandwidth is demonstrated. Here, the boundary of controller gains and outlines selection criteria based on the network time constant is elaborated. The controller system time constant is strategically chosen relative to load power and network impedance, ensuring it remains lower than the load network time constant ($\tau_s \leq \tau_n$). Under these conditions, a comparative analysis of the proposed and ripple-based filter designs is conducted across varying power levels, with %THD comparisons presented in Fig. 13. The validity of this condition is confirmed in both grid drawing and injected modes, particularly under stiff grid conditions. Fig. 13a illustrates the efficacy of harmonic compensation with the proposed filter inductance compared to diverse ripple-based filter inductance methods in grid drawing (left) and grid injected (right) modes. Additionally, Fig. 13b compares the proposed method under different controller system time constants. This reveals that a time constant lower than the network time constant yields superior harmonic compensation and lower grid current %THD.

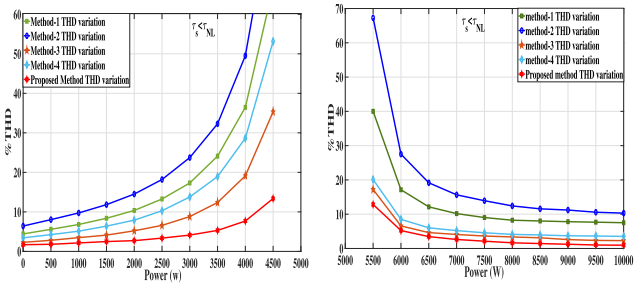

(a) THD Comparison of proposed and different filter inductances methods a) Grid drawing mode(left figure) b) Grid injection mode (right figure).

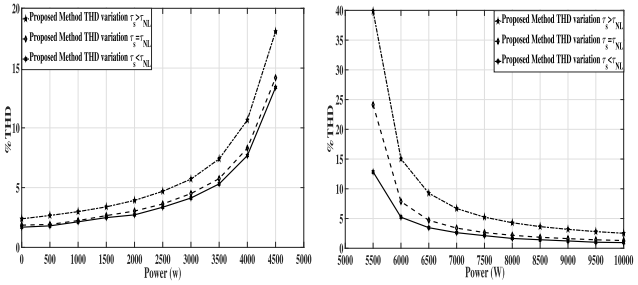

(b) THD Comparison of proposed filter inductance under different time constants with respect to load network time constant a) Grid drawing mode(left figure) b) Grid injection mode(right figure).

FIGURE 13. THD comparison of proposed and different filter inductances in grid drawing and injection modes under proposed controller gain design methods.

However, in grid injection mode, depending upon the injected power, the uncompensated grid inductance contributes to grid current oscillations, diminishing the grid's power quality. Strategies for enhancing grid power quality are discussed in the subsequent sections.

C. MODE-2 OPERATION

In this mode, the available PV power (P_S) surpasses the load power (P_L). Therefore, the excess power ($P_{gi} = P_S - P_L$) is fed into the grid after meeting the load demand. The injection into the grid is limited to the fundamental current, as the nonlinear load absorbs the harmonic currents along with the fundamental load current. Concerning the grid-injected power, the equivalent resistance can be calculated as follows:

$$R_{gi} = \frac{v_{gd}}{Avg(I_{fd} - I_{dl})} \tag{30}$$

When real power is injected into the grid, the line impedance (L_g) after the Point of Common Coupling (PCC) can induce power oscillations due to interactions between line (L_g) and filter (L_f) impedance, as illustrated in Fig. 14. These oscillations are characterized by a coupling angle (γ). Owing to the coupling angle (γ), the actual currents $I_{dact} = (I_g cos(\gamma))$ and $I_{qact} = (I_g sin(\gamma))$ never perfectly align with the reference currents (I_{dref}) and (I_{qref})), respectively. In this scenario, the power oscillations in the d-domain and q-domain for generating the reference wave can be modeled

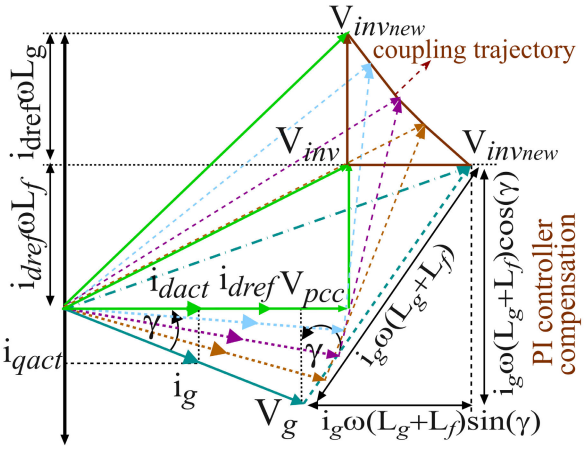

FIGURE 14. The phasor diagram representing the PCC voltage oscillations in the weak grid due to coupling angle γ in grid power injection mode.

as (32) and (33), respectively.

$$V_{inv} = V_d^* + jV_q^* \tag{31}$$

$$V_d^* = V_{d(PCC)} + (I_{dref} - I_g cos(\gamma))(K_p + \frac{K_i}{s}) \tag{32}$$

$$V_q^* = (-I_g sin(\gamma))(K_p + \frac{K_i}{s}) \tag{33}$$

Therefore, it is essential to understand the dynamics of the SiSAPF when injecting active power into the grid. This subsection aims to mitigate power oscillations in a weak grid scenario by compensating the natural deviation angle (γ) induced by grid inductance (L_g).To achieve this, the transfer function of the SiSAPF in grid injection mode is modeled as shown in Equation(34), taking into account the network impedance (L_g) and the grid power injected resistance(R_{gi}).

$$G(s) = \frac{R_{gi}.e^{-st}}{(L_g.L_f + L_g^2)(s^2 + \frac{R_{gi}.L_f.s}{L_g.L_f+L_g^2} + \frac{R_{gi}^2}{L_g.L_f+L_g^2})} \tag{34}$$

Subsequently, the characteristic equation of the closed-loop system in grid injection mode can be written as:

$$\lambda(s) = 1 + (K_P + \frac{K_i}{s}).(\frac{K.e^{-st}}{s^2 + k.L_f.s + k.R_{gi}}) \tag{35}$$

$$\lambda(s) = k(K_i + K_P.s)e^{-st} + s(s^2 + k.L_f.s + k.R_{gi}) \tag{36}$$

$$\lambda^*(s) = e^{st}.\lambda(s) \quad Where\ k = \frac{R_{gi}}{L_g^2 + L_g.L_f} \tag{37}$$

$$\lambda^*(s) = k(K_i + K_P.s) + s(s^2 + k.L_f.s + k.R_{gi})e^{st} \tag{38}$$

Later, the characteristic equation can be decomposed into real and reactive components:

$$\lambda^*(j.\omega) = \lambda_r(\omega) + j\lambda_i(\omega) \tag{39}$$

$$\lambda_r(\omega) = kK_i + (\omega^3 - kR_{gi}\omega)sin(\omega t) - \omega^2 kL_f cos(\omega t) \tag{40}$$

$$\lambda_i(\omega) = \omega(kK_P + (kR_{gi} - \omega^2)cos(\omega t) - \omega kL_f sin(\omega t) \tag{41}$$

By substituting $\omega = \gamma/t$, Equations (40) and (41) can be rewritten as:

$$\lambda_r(\gamma) = kK_i + sin(\gamma)(\frac{\gamma^3}{t^3} - \frac{a_0\gamma}{t}) - \frac{a_1\gamma^2 cos(\gamma)}{t^2}$$

$$\lambda_i(\gamma) = \frac{\gamma}{t}(kK_P + [cos(\gamma)(a_0 - \frac{\gamma^2}{t^2})] - \frac{a_1\gamma sin(\gamma)}{t}) \tag{42}$$

Here a_o=kR_{gi} and a_1=kL_f.

For any value of coupling angle (γ_0) varies from [-90°,90°], the $\lambda^*(s)$ is stable only when

(1) Condition-1: $\lambda_r(\gamma_0)$ and $\lambda_i(\gamma_0)$ have only simple and real roots and these interlace [4]

(2) Condition-2:$\dot{\lambda_i}(\gamma_0).\lambda_r(\gamma_0) - \lambda_i(\gamma_0).\dot{\lambda_r}(\gamma_0) > 0$

When establishing the lower limit of K_P through condition-2 with the evident root at γ_0=0, the condition-2 simplifies to:

$$\dot{\lambda_i}(\gamma_0).\lambda_r(\gamma_0) = (\frac{kK_P + a_0}{t})kK_i \geq 0 \tag{43}$$

Equation (43) establishes that K_P must satisfy the condition $K_P \geq \frac{-a_0}{k}$, given that both k and K_i are greater than 0.

Following that, the upper limit of K_P can be established by meeting the interlacing of roots condition as outlined in condition-1, which is only fulfilled when $\lambda_i(\gamma_0) = 0$. As a result, Equation (42) can be restructured to determine the potential roots of λ.

$$\gamma = 0 \tag{44}$$

$$kK_P + cos(\gamma)(a_0 - \omega^2) - a_1\omega sin(\gamma) = 0 \tag{45}$$

In a closed-loop controller, the parameter K_P functions as a virtual RC time constant, effectively dampening the inherent oscillations of the plant. Therefore, it is essential to initially determine the plant's natural oscillations (ω). This determination can be made using Equation (45) under the conditions $\gamma = 0$ and $K_P = 0$, as shown below:

$$\omega = \frac{R_{gi}}{\sqrt{L_g.(L_g + L_f)}}; \tag{46}$$

Alternatively, the natural oscillations can be deduced from the coupling trajectory depicted in Fig. 14. This coupling trajectory, resulting from the cross-coupling terms in the d-axis and q-axis directions, can be recognized as:

$$\frac{v_d}{i_q} = \omega(L_g + L_f) \qquad \frac{v_q}{i_d} = \omega(L_g) \tag{47}$$

The system inertial time constant corresponding to the natural oscillations can be derived as:

$$\frac{v_d}{i_q}.\frac{v_q}{i_d} = \omega^2.L_g.(L_g + L_f) \implies R_{gi}^2 = \omega^2.L_g.(L_g + L_f) \tag{48}$$

$$\omega = \frac{R_{gi}}{\sqrt{L_g.(L_g + L_f)}}; \implies \tau_g = \frac{1}{\zeta\omega} = \frac{2(L_g.(L_g + L_f))}{R_{gi}L_f} \tag{49}$$

where, $\zeta = \frac{L_f}{2\sqrt{L_g.(L_g+L_f)}}$. Here, ζ represents the damping ratio of the system, and it can be determined using

Equation (34). Additionally, τ_g denotes the time constant of the derived second-order system. Furthermore, when we substitute values of ω and γ for less than 90^o into Equation (45), we obtain:

$$K_p < L_f . \frac{R_{gi} Sin(\gamma)}{\sqrt{L_g(L_g + L_f)}} \tag{50}$$

To ensure the injection of a perfectly sinusoidal current into the grid after satisfying load demands for harmonics and active power, it's crucial to satisfy the condition $\tau_g > \tau_n$. To meet this condition, it's essential to establish a relationship between the determined value of K_P and τ_g.

$$K_P < \frac{2\sqrt{L_g(L_g + L_f)}}{\tau_g} sin(\gamma) \tag{51}$$

From Equation(51),It is clear that the value of K_P is notably influenced by τ_g, and τ_g is, in turn, dependent on τ_n.Therefore, to achieve a perfectly sinusoidal current injection into the grid, the right value for K_P is identified, ensuring that the system's time constant (τ_g) is greater than the network's time constant (τ_n). Furthermore the range of K_P value in relation to τ_g by employing Equations (43) and (51) as follows:

$$-R_{gi} \leq K_P < \frac{2\sqrt{L_g(L_g + L_f)}}{\tau_g} sin(\gamma) \tag{52}$$

D. THE SELECTION OF CONTROLLER GAINS BASED ON THE MODE OF OPERATION

This subsection emphasizes the critical role of the controller gain range in determining the closed-loop system bandwidth. This dynamic range boundary depends on the solar-injected power, illustrated in Fig. 15. In grid drawing mode, the controller gain variations are calculated within the shaded region, considering the permissible inductance value range (minimum and maximum) outlined in Section II. The pattern reveals that the gain should decrease with an increase in power, as depicted in the top trace of Fig. 15. Additionally, computed controller gains must be higher than the proportional gain corresponding to the network time constant. In grid injection mode, where the inverter processing power exceeds the load demanded power, the proportional gain limit, computed in Section IV-C, must be considered, as shown in the zoomed portion of Fig. 15. The intersection area between the upper and lower inductance values determines the total SiSAPF processing power, constrained by the grid-injected power limit. In this mode as well, it is crucial to ensure that the resultant computed gain exceeds the gain corresponding to the network time constant, as illustrated in the zoomed portion of Fig. 15. The efficacy of the SiSAPF design and closed loop controller modeling in both grid drawing and injected mode of operation is verified experimentally, and the obtained results are discussed in the following section.

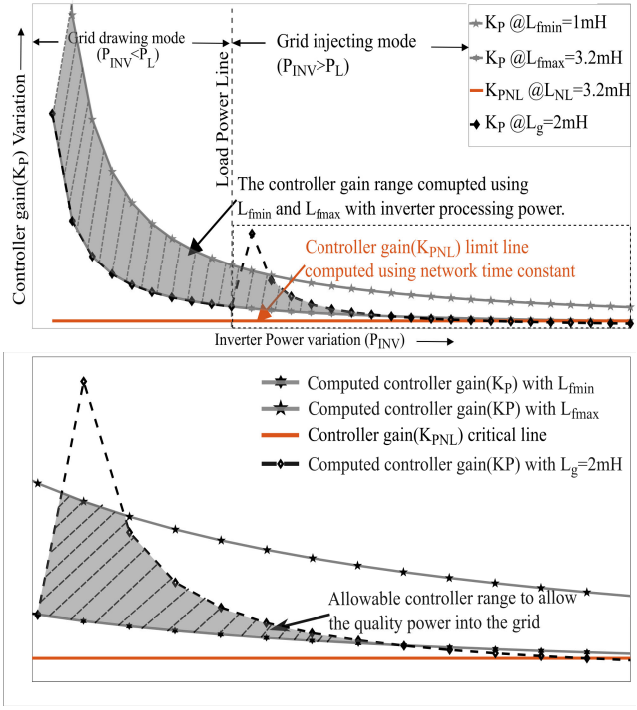

FIGURE 15. a) Allowable controller range for the SiSAPF from minimum to maximum controller gain with respect to when the system changes from grid drawing mode to grid injection mode. b) The zoomed portion of the grid-injected mode region to ensure the limit for the grid-injected power.

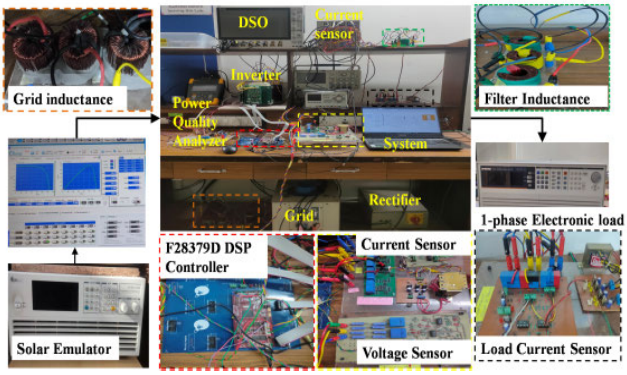

FIGURE 16. The SiSAPF hardware prototype developed in the lab.

V. RESULTS AND DISCUSSION

This analysis is confirmed by developing the SISAPF lab prototype, illustrated in Fig. 16. Design parameters for harmonic compensation and active power injection in the SISAPF prototype are provided in Table-1. Furthermore, the experimental section discusses the effect of controller gains on the computed inductance range during harmonic compensation and active power injection in both grid drawing and injection modes, as previously mentioned.

In this work, a nonlinear load represented by an AC/DC rectifier is demonstrated using a DC load resistance of $R_L = (18.67(\mathbb{R}) \times 1.823)\Omega$. Initially, this load is powered by the utility grid supply. The rise time of the load current is

TABLE 1. Specifications of filter design.

PCC voltage = 121 V (L-L RMS), load output voltage = 163.74 V Load Power(P_L)=787.39 W, Load input Current (I_L)=3.75 A, Inverter Power(P_S)= 1500 W, Inverter current (I_f)= 7.143 A, load equivalent resistance($\mathbb{R} = R_{NL}$) = 18.67.

	General filter	Proposed filter
filter design (L_f)	$L_f = \frac{V_{dc}}{8F_{sw}\triangle I_{pp}}$	$L_f = \frac{\mathbb{R}}{2\pi f_{sw}}$
DC-link voltage (V_{dc})	300 V	300 V
modulation index (M_a)	1	1
Switching Frequency (F_{sw})	5KHz	5KHz
current ripple ($\triangle I_{pp}$)	10%	-
Filter inductance (L_f)	10.49 mH	0.594 mH $\approx$ 0.6mH

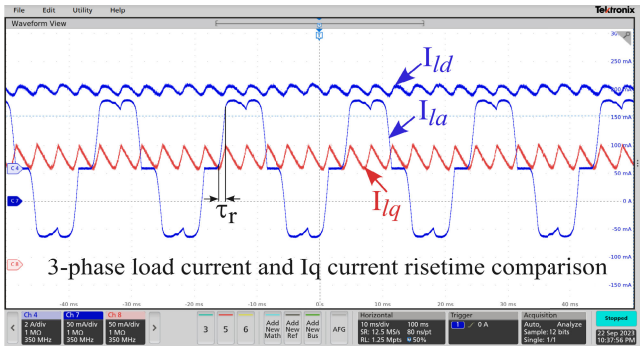

FIGURE 17. The a-phase non linear load current (X-limit: 2A/div, Y-limit: 10ms/div) along with equivalent current correspond to real (i_{dl}) and reactive power (i_{ql}) (X-axis: 50mA/div, Y-axis: 10ms/div).

observed and compared in both stationary (a-phase current) and synchronous reference frame (I_{ld} and I_{lq}), as depicted in Fig.17, to calculate the network time constant (τ_n).

From Fig. 17, it's clear that the rise time of the nonlinear load diode current during the off-to-on transition precisely matches that of the load current's reactive component, I_{lq}, which is 0.416ms (τ_r). Using this derived rise time, the network time constant can be computed as $\frac{\tau_r}{2.197}$, resulting in 0.1896ms. Notably, this computed load network time constant, based on the rise time at a load inductance of L_{NL} = 3.2mH and resistance of $\mathbb{R}$ = 18.675Ω, aligns with the calculated network time constant (τ_n). This confirms the accuracy of the measurement-based network time constant computation and its independence from specific parameters. With the specified load inductance and resistance, the grid current % THD is measured at 22.6% (without compensation), as seen in Fig. 18. Using the computed network time constant and network equivalent resistance, the filter inductance for SiSAPF is determined to be 0.6mH.

Based on the network time constant, the computed passive filter design for SISAPF harmonic compensation is compared

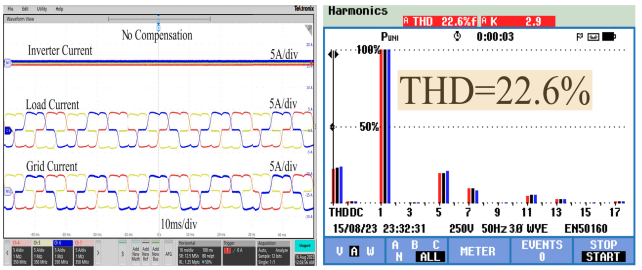

FIGURE 18. The 3-phase inverter currents (top trace), load currents (Middle trace), and grid currents (bottom trace) with no compensation from the SiSAF (Left) and corresponding grid current harmonic spectrum (Right).

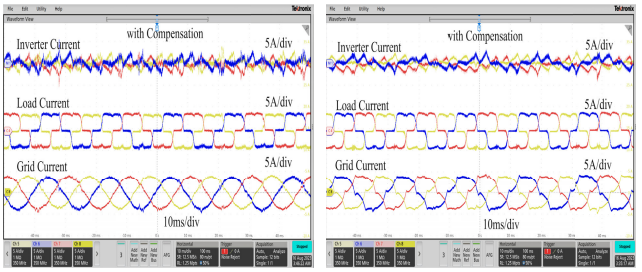

(a) The three-phase Inverter currents (top trace), load currents (Middle trace), and grid currents (bottom trace) (X-limit: 5A/div, Y-limit: 10ms/div).

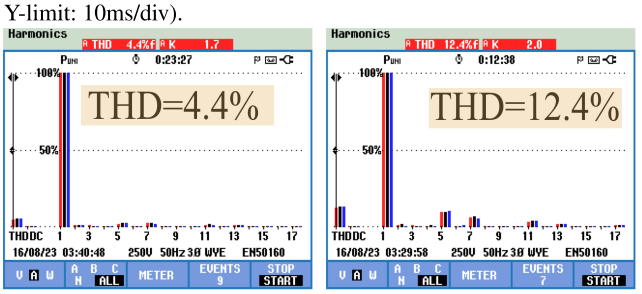

(b) The Grid current harmonic spectrum with %THD.

FIGURE 19. The experimental comparison when SiSAPF operates in harmonic compensation mode with Filter inductance L_f = 0.6*mH* computed through the proposed method (left figure) and L_f = 10*mH* computed using ripple-based filter design (Right figure).

with the conventional ripple-based filter and detailed in Table-1. With the calculated filter parameters, the SISAPF was tested experimentally, and the current waveforms of the SISAPF, load, and grid are shown in Fig. 19a. In Fig. 19b, the conventional method exhibits visible notches in the grid current, reducing grid current THD to 12.4%. In contrast, the proposed method effectively compensates for these notches in the grid current, reducing the grid current THD to 4.4% as illustrated in Fig. 19b. This improvement is attributed to the smaller filter inductance in the proposed design, providing a wider bandwidth for accommodating load-demanded harmonics compared to the ripple-based design with higher inductance. Additionally, the computed system time constant is lower than the network time constant, allowing the passive filter design to increase the filter value to align with the network time constant. The effectiveness of the minimum and maximum boundaries specified in the proposed filter inductance design methodology

TABLE 2. The Nonlinear load network parameters along with SiSAPF system parameters at different SiSAPF's operating modes.

Network Parameters		Grid drawing mode		grid injected mode	
		$P_S < P_L$		$P_S > P_L$	
grid side inductance(L_{NL})	3.2mH	Inverter power (P_S)	790 w	Inverter power (P_S)	1500 w
load resistance(R_L)	18.68Ω	Equivalent resistance ($\mathbb{R}_2$)	18.68Ω	Grid power(P_{gi})	712 w
time constant (τ_n)	0.1713 msec	switching frequency (f_{sw})	5kHz	Switching frequency (f_{sw})	5kHz
load Power (P_L)	790 W	minimum filter inductance ($L_{f_{min}}$)	0.594mH	grid side inductance(L_g)	3.2mH
fundamental Frequency(F_n)	50Hz	$\tau_{min} = L_{f_{min}}/R_2$ & $\tau_{max} = L_{f_{max}}/R_2$	0.03183 msec & 0.1713 msec	filter inductance ($L_{f_{min}}$)	0.594mH
		Maximum filter inductance($L_{f_{max}}$)	3.2mH	filter inductance ($L_{f_{max}}$)	3.2mH
		Kp at $L_{f_{min}}$ (K_P for controller @ $Z_{base} = 18.68\Omega$) & Kp with$L_{f_{max}}$ (K_P for controller @ $Z_{base} = 18.68\Omega$)	3.46 (0.2)& 18.68 (1.0)	Kp with L_{fmin}	3.46 (0.2)

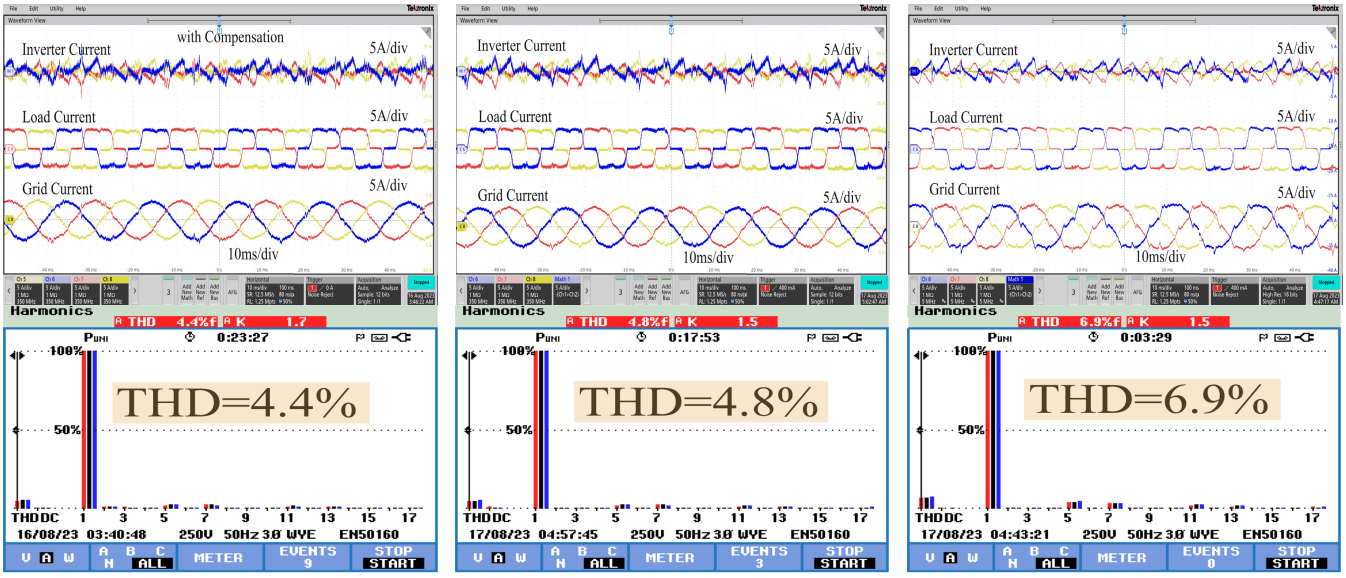

(a) $L_f = L_{fmin} = 0.6mH.$ (b) $L_f = L_{fmax} = 3mH.$ (c) $L_f > L_{fmax} = 6mH.$

FIGURE 20. The effect of different filter inductances on SiSAPF circuit and grid current THD. The SiSAPF current (top trace X=10ms/div, Y=5A/div), nonlinear load current(middle trace X=10ms/div, Y=5A/div), and grid current(bottom trace X=10ms/div, Y=5A/div). Zoomed portions correspond to the grid current waveform THDs, respectively.

(Section-III) is validated for simultaneous harmonic compensation and power injection in both grid drawing and injection modes, utilizing the network parameters detailed in Table-2.

The influence of the computed passive filter inductance range on the grid current's %THD is experimentally shown in Fig. 20. In the left figure of Fig. 20, the minimum filter inductance maintains %THD at 4.4%, while the maximum

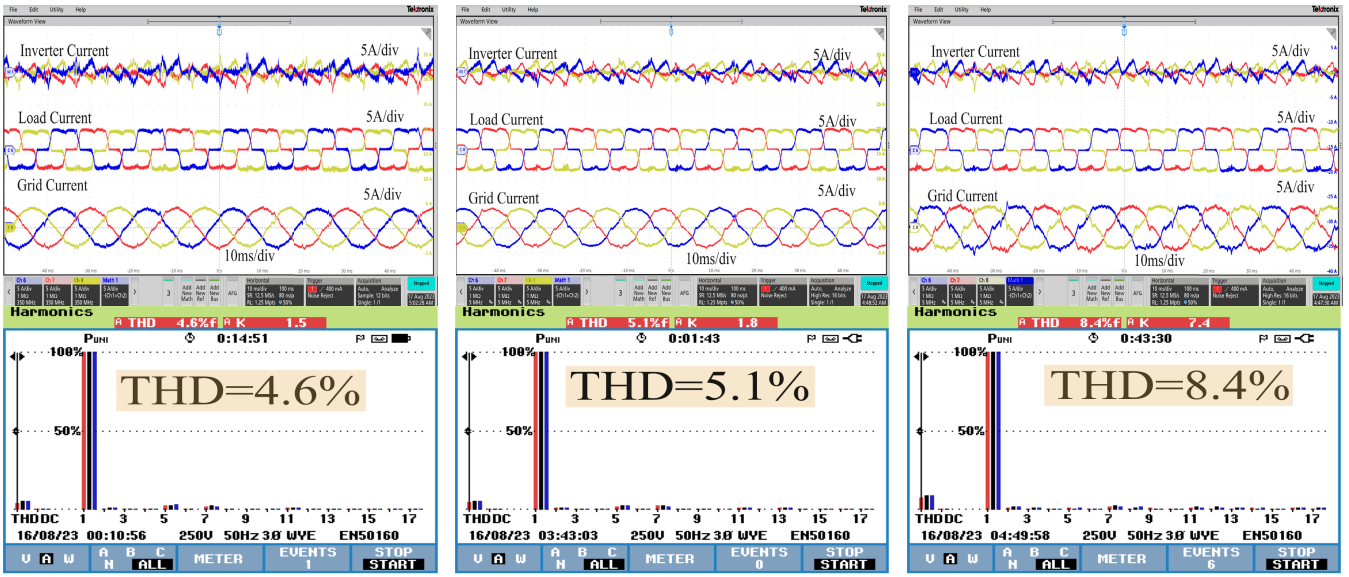

(a) $\tau_s(0.05msec) < \tau_n(0.1713msec)$. (b) $\tau_s(0.1713msec) = \tau_n(0.1713msec)$. (c) $\tau_s(0.2msec) > \tau_n(0.1713msec)$.

FIGURE 21. The effect of different system time constant over network time constant for SiSAPF circuit on grid current THD. In the Top figure, SiSAPF current (top trace X=10ms/div, Y=5A/div), nonlinear load current(middle trace Y=5A/div), and grid current(bottom trace Y=5A/div) for one designed filter inductance and their corresponding grid current THD (bottom figures).

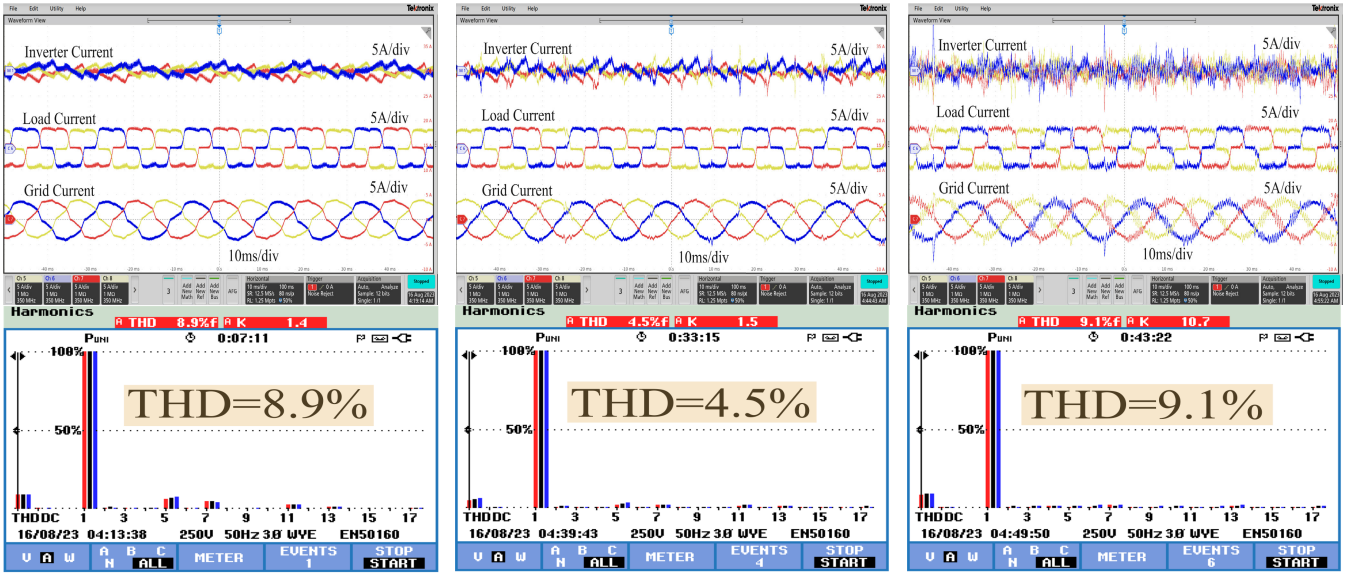

(a) $K_P < K_{Pcomputed} = 0.1P.U.$ (b) $K_P = K_{Pcomputed} = 0.22P.U.$ (c) $K_P > K_{Pcomputed} = 1.2P.U.$

FIGURE 22. The effect of different controller gains on SiSAPF circuit and grid current THD. In the Top figure, SiSAPF current (top trace X=10ms/div, Y=5A/div), nonlinear load current(middle trace X=10ms/div, Y=5A/div), and grid current(bottom trace X=10ms/div, Y=5A/div) for one designed filter inductance.

filter inductance keeps it at 4.8%. However, when the filter inductance surpasses this range, notches appear in the grid current, resulting in a higher %THD of 6.9%. This indicates that the SiSAPF cannot provide the necessary high-frequency components through the inverter circuit to meet load demands.

To design the controller gains, the consideration of the system time constant(τ_s) is crucial, and the system time constant should be less than the network time constant(τ_n). For practical experimentation, the SiSAPF is validated with the various time constants, as depicted in Fig. 21. The system constant is lesser than the network time constant ($\tau_s = 0.05msec < \tau_n$), as shown in Fig. 21a, which effectively compensates the harmonics and reduces the grid current %THD to 4.6%. Incase, at system time constant is equal to network time constant ($\tau_s = 0.1713msec = \tau_n$)as

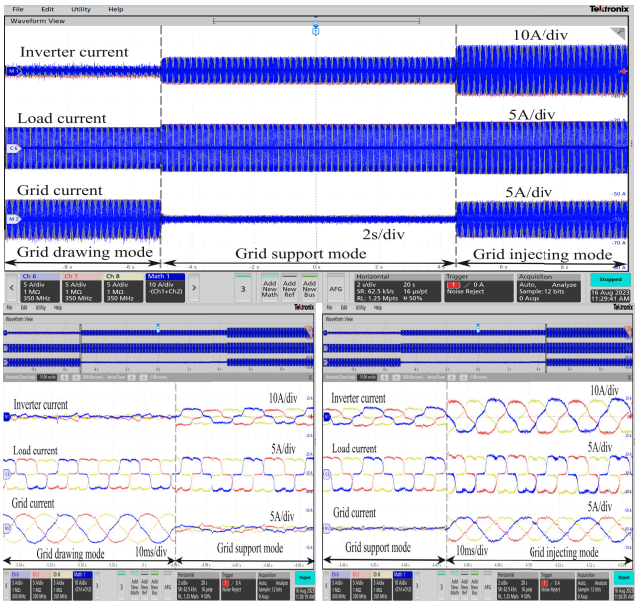

FIGURE 23. The SiSAPF current(top trace X=2sec/div, Y=10A/div), three-phase non-linear load current(middle trace Y=5A/div), and grid current(bottom trace Y=5A/div). The zoomed portions correspond to the dynamic variation of SASAF power from 10 W to 790 W(left figure X=10msec) and 790 W to 1400 W(right figure).

shown in Fig. 21b, The bandwidth for the load demanded harmonics is reduced, which starts degrading the grid current quality, and increase the %THD to 5.1%. Conversely, at a higher time constant ($\tau_s = 0.2msec > \tau_n$), as shown in Fig. 21c, the controller bandwidth is not sufficient to compensate for the grid current, resulting in an increase of grid current %THD to 8.4%. Considering the different time constants for computing the controller gains for the effective harmonic compensation, the system constant should vary between (τ_{min} *to* τ_n). Furthermore, the effect controller gains on harmonic compensation is discussed in the following paragraph.

The controller gains for SiSAPF at the computed minimum and maximum filter inductance are assessed, and the results are presented in Table-2. The practical effectiveness of these evaluated gains is experimentally validated across various controller gain settings using the computed passive filter for SiSAPF, as demonstrated in Fig. 22. A controller gain lower than the computed K_p (0.1PU), as seen in Fig. 22a, causes notches in the grid current due to insufficient controller bandwidth, causing an increase in % THD to 8.9%. At the computed K_p, as shown in Fig. 22b, the controller provides sufficient bandwidth to mitigate load-demanded harmonics, reducing grid current % THD to 4.5%. Conversely, higher K_p results in a grid current % THD of 9.1%, as seen in Fig. 22c. While higher controller gains improve the system's dynamic response, they lead to peak overshoots and negatively impact current quality, considering the load network time constants. Further, the computed controller gain and passive filter observe the dynamic change in the source power.

The effectiveness of SiSAPF in handling dynamic changes in source power is demonstrated in Fig. 23. The system's

TABLE 3. Considered parameters for weak grid condition experimentation.

grid voltage = 230 V, PCC voltage= 140 V, DC-link voltage= 400 V, load Power(P_L)=1500 W, load current= 3.57 A, Inverter Power(P_S)= 3000 W, Inverter current (I_f)= 6.66 A, $\mathbb{R} = 39.2\Omega$, network inductanceL_{NL}=3.2mH, Time constant(τ_n=0.0816msec).

Grid inductance (L_g)	14.5mH
internal resistance of inductance	3.5 Ω
filter inductanceL_{fmax}	3.2 mH
Controller gain ($K_P@L_{fmax}$)	1 P.U
Controller gain (K_{Pweak})	0.2 P.U
Fundamental frequency(F_n)	50 Hz

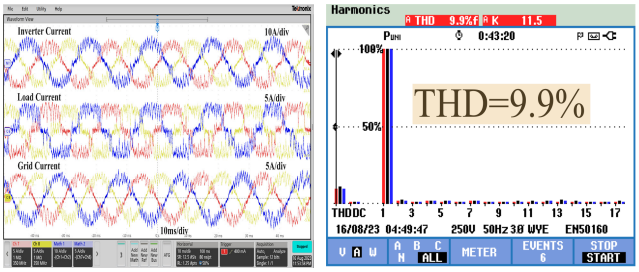

(a) With the controller gain outside the recommended area as described in Fig. 15

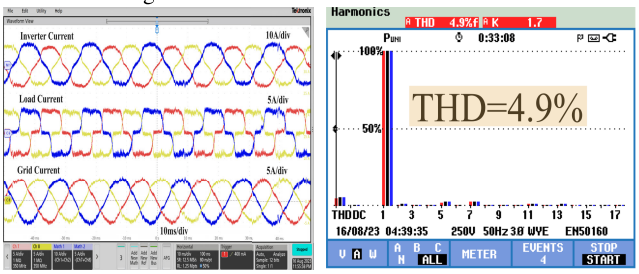

(b) With the controller gain falls within the recommended area as described in Fig. 15

FIGURE 24. The SiSAPF current(top trace X=10ms/div, Y=10A/div), three-phase load current(middle trace Y=5A/div), and grid current(bottom trace Y=5A/div) and corresponding grid injected current %THD with mimicked weak grid condition.

dynamic response is showcased as the source power varies from 10W to 790W and then from 790W to 1500W. In the dynamic characteristics, both grid drawing ($P_s < P_L$) and grid injection modes are displayed while maintaining the load at 790W, as shown in the zoomed left and right traces of Fig. 23. In both cases, the grid currents remain sinusoidal, affirming the efficacy of the SiSAPF filter design across different power ranges. Additionally, the power injection limit concerning controller gains due to uncompensated grid inductance is demonstrated, as discussed in Section-IV-C.

The grid inductance (Lg) is emulated in the grid line to create a weak grid with a short circuit ratio (SCR) between 2 and 3. The experimental parameters in Table-3 for validate the injected power quality at varying controller gains, as shown in Fig.15. Under the emulated weak grid conditions, experiments are conducted with controller gains falling both outside and inside the intersection area described in Fig. 15,

and the results are depicted in Fig. 24a. When the gain is outside the designated area ($K_p > K_{pweak}$), such as at K_p = 2 PU, oscillations occur due to impedance interactions, resulting in elevated grid-injected current %THD (9.9%), as seen in the harmonic spectrum in Fig. 24b. These oscillations can be suppressed with the appropriate selection of controller gain, as computed in Table-3 ($K_{pweak} = 0.2$ P.U), as evidenced by the experimental results in Fig. 2b. With the computed controller gain, grid current distortions are mitigated, leading to an improved grid current THD of 4.9%. This discussion highlights the adverse impact of exceeding threshold controller values on grid power quality in accordance with IEEE standards.

VI. CONCLUSION

This work demonstrates a solar-interfaced shunt active filter for supplying active power and mitigating nonlinear load harmonics from grid current. The nonlinear load current harmonics are addressed using a synchronous reference frame, and the controller's reactive power component is observed to encompass the three-phase load current bandwidth. The load network's time constant is determined based on the rise time of the reactive power component. This identified network time constant discusses and analyzes an effective filter design. Compared to ripple-based filter designs, the proposed filter design offers a wider bandwidth, significantly enhancing grid current quality by reducing %THD from 22.6% to 4.4%. The closed-loop controller gains are computed using the determined network time constant and filter design to shape the grid current into a pure sinusoidal pattern. During grid power drawing operation, the filter inductance and proportional controller gains are adjusted to match the required network time constant, ensuring that the grid current quality remains within IEEE standards. In the grid-injected operation mode, interactions with the grid inductance due to injected power are modeled to understand the effect of injected power quality. Consequently, appropriate controller gain tuning dampens oscillations induced by system inductance, maintaining THD within IEEE standards in grid-injected mode.

APPENDIX: REALIZATION OF LOAD IMPEDANCE AT PCC

In the present work, the impedance offered by the non-linear load at AC or PCC terminals must be considered in the design methodology. The mathematical formulation relating DC and AC side load impedances is shown below.

On ignoring the rectification loss.

$$P^{L}_{load} = P^{NL}_{load} \tag{53}$$

$$V_L I_L = 3 V_{L-N} I_{L-N} \tag{54}$$

Here, the AC side three-phase configuration is assumed to be a star connection. On substituting, $V_L = \frac{3\sqrt{6}}{\pi} V_{L-N}$ in (54),

$$I_L = \frac{\pi}{\sqrt{6}} I_{L-N} \tag{55}$$

The Equivalent resistances on the DC and AC sides are,

$$R_L = \frac{V_L}{I_L}$$

$$R_{NL} = \frac{V_{L-N}}{I_{L-N}}.$$

Substitute V_L and I_L expressions in R_L and proceed to obtain the relationship with AC side impedance. On simplification,

$$R_L = \frac{18}{\pi^2} R_{NL}. \tag{56}$$

REFERENCES

[1] A. A. Jai and M. Ouassaid, "Machine learning-based adaline neural PQ strategy for a photovoltaic integrated shunt active power filter," *IEEE Access*, vol. 11, pp. 56593–56618, 2023.

[2] D. Çelik, H. Ahmed, and M. E. Meral, "Kalman filter-based super-twisting sliding mode control of shunt active power filter for electric vehicle charging station applications," *IEEE Trans. Power Del.*, vol. 38, no. 2, pp. 1097–1107, Apr. 2023.

[3] S. S. Sayed and A. M. Massoud, "Review on state-of-the-art unidirectional non-isolated power factor correction converters for short-/long-distance electric vehicles," *IEEE Access*, vol. 10, pp. 11308–11340, 2022.

[4] B. K. Gupta, K. R. Sekhar, and A. I. Gedam, "Solar interfaced series inverter with provision of common DC bus grounding," *IEEE Trans. Ind. Electron.*, vol. 69, no. 4, pp. 3656–3666, Apr. 2022.

[5] R. K. Agarwal, I. Hussain, and B. Singh, "Implementation of LLMF control algorithm for three-phase grid-tied SPV-DSTATCOM system," *IEEE Trans. Ind. Electron.*, vol. 64, no. 9, pp. 7414–7424, Sep. 2017.

[6] B. Singh, M. Kandpal, and I. Hussain, "Control of grid tied smart PV-DSTATCOM system using an adaptive technique," *IEEE Trans. Smart Grid*, vol. 9, no. 5, pp. 3986–3993, Sep. 2018.

[7] "*IEEE Recommended Practice and Requirements for Harmonic Control in Electric Power Systems*, IEEE Standard 519-2014 (Revision of IEEE Std 519-1992), 2014, doi: 10.1109/IEEESTD.2014.6826459.

[8] K. Jalili and S. Bernet, "Design of *LCL* filters of active-front-end two-level voltage-source converters," *IEEE Trans. Ind. Electron.*, vol. 56, no. 5, pp. 1674–1689, May 2009.

[9] M. Liserre, F. Blaabjerg, and S. Hansen, "Design and control of an LCL-filter-based three-phase active rectifier," *IEEE Trans. Ind. Appl.*, vol. 41, no. 5, pp. 1281–1291, Oct. 2005.

[10] H. Akagi, E. H. Watanabe, and M. Aredes, *Instantaneous Power Theory and Applications to Power Conditioning*, 2nd ed. New York, NY, USA: Wiley,2017.

[11] H. Akagi, Y. Kanazawa, and A. Nabae, "Instantaneous reactive power compensators comprising switching devices without energy storage components," *IEEE Trans. Ind. Appl.*, vol. IA-20, no. 3, pp. 625–630, May 1984.

[12] Y. Hoon, M. A. M. Radzi, M. K. Hassan, and N. F. Mailah, "Operation of three-level inverter-based shunt active power filter under nonideal grid voltage conditions with dual fundamental component extraction," *IEEE Trans. Power Electron.*, vol. 33, no. 9, pp. 7558–7570, Sep. 2018.

[13] G. A. D. A. Carlos, C. B. Jacobina, E. C. dos Santos, E. L. L. Fabrício, and N. Rocha, "Shunt active power filter with open-end winding transformer and series-connected converters," *IEEE Trans. Ind. Appl.*, vol. 51, no. 4, pp. 3273–3283, Jul. 2015.

[14] A. Fereidouni, M. A. S. Masoum, and K. M. Smedley, "Supervisory nearly constant frequency hysteresis current control for active power filter applications in stationary reference frame," *IEEE Power Energy Technol. Syst. J.*, vol. 3, no. 1, pp. 1–12, Mar. 2016.

[15] Q.-N. Trinh and H.-H. Lee, "An advanced current control strategy for three-phase shunt active power filters," *IEEE Trans. Ind. Electron.*, vol. 60, no. 12, pp. 5400–5410, Dec. 2013.

[16] S. Rahmani, N. Mendalek, and K. Al-Haddad, "Experimental design of a nonlinear control technique for three-phase shunt active power filter," *IEEE Trans. Ind. Electron.*, vol. 57, no. 10, pp. 3364–3375, Oct. 2010.

[17] X. Nie and J. Liu, "Current reference control for shunt active power filters under unbalanced and distorted supply voltage conditions," *IEEE Access*, vol. 7, pp. 177048–177055, 2019.

[18] A. K. Mishra, S. R. Das, P. K. Ray, R. K. Mallick, A. Mohanty, and D. K. Mishra, "PSO-GWO optimized fractional order PID based hybrid shunt active power filter for power quality improvements," *IEEE Access*, vol. 8, pp. 74497–74512, 2020.
[19] P. M. Reddy, K. Manjunath, K. R. Sekhar, and B. K. Gupta, "Nonlinear load time-constant based filter inductance design for PV-driven grid-connected SAF/PFC in EV charging infrastructure," in *Proc. 49th Annu. Conf. IEEE Ind. Electron. Soc.*, Singapore, Oct. 2023, pp. 1–6.
[20] R. Musa, A. Hamadi, A. Ndtoungou, S. Rahmani, and K. Al-Haddad, "Optimal design of inductor and DC bus voltage for shunt active filter," in *Proc. 43rd Annu. Conf. IEEE Ind. Electron. Soc.*, Oct. 2017, pp. 6482–6487.
[21] A. M. Al-Zamil and D. A. Torrey, "A passive series, active shunt filter for high power applications," *IEEE Trans. Power Electron.*, vol. 16, no. 1, pp. 101–109, Jan. 2001.
[22] H. Chen, H. Liu, Y. Xing, and H. Hu, "Enhanced DFT-based controller for selective harmonic compensation in active power filters," *IEEE Trans. Power Electron.*, vol. 34, no. 8, pp. 8017–8030, Aug. 2019.
[23] M. Golla, S. Thangavel, S. P. Simon, and N. P. Padhy, "A novel control scheme using UAPF in an integrated PV grid-tied system," *IEEE Trans. Power Del.*, vol. 38, no. 1, pp. 133–145, Feb. 2023.
[24] M. Golla, S. Thangavel, S. P. Simon, and N. P. Padhy, "An enhancement of power quality with efficient active power transfer capability in a PV–BSS-fed UAPF for microgrid realization," *IEEE Syst. J.*, vol. 17, no. 1, pp. 1614–1625, Mar. 2023.
[25] R. Guzman, L. G. de Vicuña, J. Morales, M. Castilla, and J. Miret, "Model-based control for a three-phase shunt active power filter," *IEEE Trans. Ind. Electron.*, vol. 63, no. 7, pp. 3998–4007, Jul. 2016.
[26] S. Hou, J. Fei, Y. Chu, and C. Chen, "Experimental investigation of adaptive fuzzy global sliding mode control of single-phase shunt active power filters," *IEEE Access*, vol. 7, pp. 64442–64449, 2019.
[27] J. Morales, L. G. de Vicuña, R. Guzman, M. Castilla, and J. Miret, "Modeling and sliding mode control for three-phase active power filters using the vector operation technique," *IEEE Trans. Ind. Electron.*, vol. 65, no. 9, pp. 6828–6838, Sep. 2018.
[28] M. Pichan, M. Seyyedhosseini, and H. Hafezi, "A new DeadBeat-based direct power control of shunt active power filter with digital implementation delay compensation," *IEEE Access*, vol. 10, pp. 72866–72878, 2022.
[29] L. Zhou, Z. Zhou, J. Qi, and W. Han, "Hybrid prediction-based deadbeat control for a high-performance shunt active power filter," *IEEE Access*, vol. 11, pp. 11118–11131, 2023.
[30] L. Yang, L. Zhao, X. Chen, Z. Zhang, H. Nian, J. Zhao, R. Deng, and L. Yan, "Robust active damping control for LCL-type shunt active power filters," *IEEE Access*, vol. 10, pp. 39456–39470, 2022.
[31] N.-Y. Dai and M.-C. Wong, "Design considerations of coupling inductance for active power filters," in *Proc. 6th IEEE Conf. Ind. Electron. Appl.*, Jun. 2011, pp. 1370–1375.
[32] W. Wu, Y. Liu, Y. He, H. S.-H. Chung, M. Liserre, and F. Blaabjerg, "Damping methods for resonances caused by LCL-filter-based current-controlled grid-tied power inverters: An overview," *IEEE Trans. Ind. Electron.*, vol. 64, no. 9, pp. 7402–7413, Sep. 2017.
[33] B. K. Gupta and K. R. Sekhar, "A current controller gain characterization of weak grid coupled solar inverter through impedance interaction modeling," *IEEE Trans. Ind. Electron.*, vol. 70, no. 3, pp. 2520–2530, Mar. 2023.
[34] J. Fang, X. Li, H. Li, and Y. Tang, "Stability improvement for three-phase grid-connected converters through impedance reshaping in quadrature-axis," *IEEE Trans. Power Electron.*, vol. 33, no. 10, pp. 8365–8375, Oct. 2018.
[35] B. Wen, D. Dong, D. Boroyevich, P. Mattavelli, R. Burgos, and Z. Shen, "Impedance-based analysis of grid-synchronization stability for three-phase paralleled converters," *IEEE Trans. Power Electron.*, vol. 31, no. 1, pp. 26–38, Jan. 2016.
[36] X. Zhang, D. Xia, Z. Fu, G. Wang, and D. Xu, "An improved feedforward control method considering PLL dynamics to improve weak grid stability of grid-connected inverters," *IEEE Trans. Ind. Appl.*, vol. 54, no. 5, pp. 5143–5151, Sep. 2018.

P. MAHESH REDDY (Member, IEEE) received the B.Tech. degree in electrical and electronics engineering from the ACE Engineering College, JNTUH, Hyderabad, India, in 2016, and the M.E. degree in electrical engineering from the Vasavi College of Engineering, Osmania University, Hyderabad, in 2018. He is currently pursuing the Ph.D. degree with the Electrical Engineering Department, Indian Institute of Technology Ropar, India. His research interests include design and implementation of high power density renewable converters and corresponding control techniques for the power converter, active filters, power quality, and regenerative braking drives.

BAIBHAV KUMAR GUPTA received the B.Tech. degree in electrical and electronics engineering, in 2013, the M.E. degree in electrical engineering, in 2016, and the Ph.D. degree from the Indian Institute of Technology Ropar, India, in 2023. He is currently a Research Associate with the Electrical Department, Indian Institute of Technology Ropar. His research interests include design and implementation of high power density renewable converters and corresponding control techniques, power quality, and stability analysis of power networks.

K. RAMACHANDRA SEKHAR (Member, IEEE) received the B.E. degree in electrical and electronics engineering from the University of Madras, Chennai, India, in 2004, the M.E. degree in power electronics and drives from Anna University, Chennai, in 2006, and the Ph.D. degree from the Indian Institute of Technology Hyderabad, India, in 2013. From 2013 to 2017, he was with the Hitachi Research and Development Division, as a Researcher. Since 2017, he has been an Assistant Professor with the Electrical Department, Indian Institute of Technology Ropar. His research interests include design and implementation of high energy density converters for utility grid/micro-grid, control techniques for the power converter, power quality assessment, and EMC/EMI analysis.